Ultrafast strain excitation in highly magnetostrictive terfenol: Experiments and theory

T. Parpiiev,[1,*] A. Hillion,[2] V. Vlasov,[1] V. Gusev,[3] K. Dumesnil,[2] T. Hauet,[2] S. Andrieu,[2] A. Anane,[4] and T. Pezeril[1,5,6,†]

[1]*Institut Molécules et Matériaux du Mans, UMR CNRS 6283, Le Mans Université, 72085 Le Mans, France*

[2]*Institut Jean Lamour, UMR CNRS 7198, Université de Lorraine, 54506 Vandoeuvre, France*

[3]*Laboratoire d'Acoustique de l'Université du Mans, UMR CNRS 6613, Institut d'Acoustique - Graduate School, Le Mans Université, 72085 Le Mans, France*

[4]*Unité Mixte de Physique CNRS/Thales, UMR CNRS 137, 91767 Palaiseau, France*

[5]*Institut de Physique de Rennes, UMR CNRS 6251, Université Rennes 1, 35042 Rennes, France*

[6]*Department of Chemistry, Massachusetts Institute of Technology, Cambridge, MA 02139, USA*

(Received 22 June 2021; revised 10 December 2021; accepted 13 December 2021; published 22 December 2021)

We experimentally and analytically investigate laser excitation of picosecond longitudinal and shear acoustic pulses in highly magnetostrictive terfenol-$TbFe_2$-epitaxial thin films. We report a magnetoelastic mechanism for picosecond longitudinal and shear acoustic strain excitation, so-called direct transient demagnetostriction, which denotes the ultrafast laser-induced demagnetization and release of static magnetostrictive built-in strains. From analytical considerations and numerical modeling, we demonstrate that the efficiency of ultrashort longitudinal and shear acoustic strains generation strongly depends on the magnetization orientation with respect to the lattice crystallographic directions. Overall, our study provides insight into ultrafast acoustic waves excitation and detection in all sorts of magnetic materials from laser-based mechanisms.

DOI: 10.1103/PhysRevB.104.224426

I. INTRODUCTION

Ultrafast optical studies of nanoscale magnetic materials at femtosecond timescales have arisen great attention over the past decades, from both fundamental and technological standpoints. Numerous investigations have been performed in order to understand ultrafast loss of spin order and disentangle complex interplay between electrons, spins and phonons during laser-matter interaction processes [1–7]. A variety of different microscopic models have been proposed to explain ultrafast demagnetization [8,9]. Results demonstrating all-optical switching in a broad variety of rare-earth–transition metal compounds with pronounced magnetostriction [10–12] challenge present theories and arise fundamental questions about the role of the ultrafast spin-lattice coupling mechanism in such type of magnetostrictive compounds. Similarly, the role of GHz-THz acoustic phonons emission during the demagnetization/remagnetization process, the manipulation of magnetization precession and even magnetization reversal from acoustic strain pulses in magnetically ordered materials is getting more and more attention [13–23].

Unlike longitudinal acoustic waves, that are efficiently excited via transient laser heating [24] or other mechanisms [25], excitation of ultrafast shear acoustic waves implies more sophisticated experimental configurations that are most often not efficient in the THz frequency range [26]. Efficient, high frequencies up to THz, short nanometer wavelengths, shear acoustic transducers are lacking for the fundamental study of the viscoelastic properties of disordered and partially ordered systems such as supercooled liquids and glasses, multiferroics or other correlated electron systems in which fast relaxation dynamics or mesoscopic correlation lengths of quantities that are coupled to shear play important roles. Recently, femtosecond time-resolved x-ray diffraction experiments have shown that laser-induced demagnetization of ferromagnetic iron is transferred to the lattice on subpicosecond timescales, launching a shear strain wave that propagates from the surface into the bulk [27]. These findings have been interpreted as the occurrence of the ultrafast Einstein-de Haas effect, however, anytime a compound exhibits static magnetoelastic coupling such as quadratic magnetostriction, the key role of (de)magnetostriction for the efficient ultrafast laser-excitation of shear acoustic strains should be considered as well. Similarly, earlier ultrafast experiments based on canted ferromagnetic iron thin films [28] have proven the efficient excitation of laser-driven shear acoustic waves from an elusive mechanism, not investigated thoroughly at that time, that might be linked with (de)magnetostriction.

In the present paper, we experimentally and theoretically scrutiny the ultrafast laser-induced mechanisms for longitudinal and shear excitation in magnetostrictive materials. We first describe femtosecond optical experiments performed in highly magnetostrictive terfenol-$TbFe_2$-epitaxial thin films. The experimental results suggest the excitation of shear acoustic strains from ultrafast direct magnetostriction—optically induced release of built-in static magnetostrictive strains in terfenol thin film leads to excitation of shear acoustic waves. To account for the possible ultrafast shear excitation in magnetostrictive compounds, we develop an

*Present address: Department of Chemistry, University of California, Berkeley, California 94720, USA.

†pezeril@mit.edu

 ©2021 American Physical Society

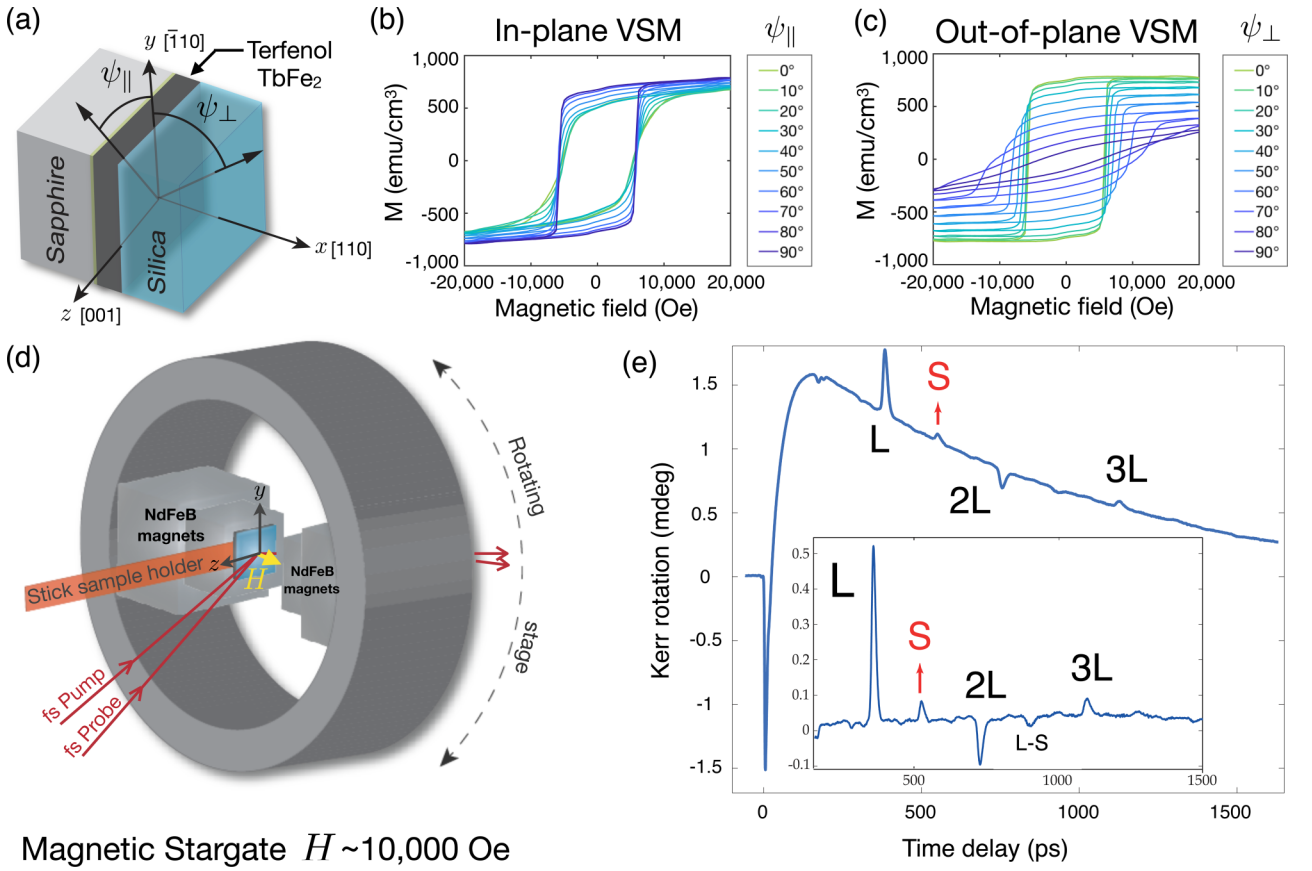

FIG. 1. (a) Typical sample structure composed of a dielectric vitreous SiO_2 thin film, a single crystal magnetic $TbFe_2$ layer with in-plane easy axis of magnetization $\vec{M}$, a Nb buffer layer, a sapphire substrate. (b) In-plane (0° corresponds to [001] and 90° corresponds to [$\bar{1}$10] directions) (c) out-of-plane (0° corresponds to [$\bar{1}$10] and 90° corresponds to [110] directions) VSM hysteresis loops in case of a 50 nm Nb/300 nm $TbFe_2$/1100 nm SiO_2 multilayer sample. (d) The sample is placed inside the "magnetic stargate" holder, under a static out-of-plane external magnetic field H of at least ±7.5 kOe. (e) Corresponding time-resolved differential MOKE signal from the same sample. Inset shows background-free differential signal $+H - (-H)$ and highlights acoustic echoes of different longitudinal (L) and supposedly shear (S) acoustic polarizations. Measurements were performed at room temperature.

analytical model that lay the groundwork for future studies of ultrafast magnetoelastic coupling. The present theory sheds light on efficient magnetoelastic mechanisms for GHz-THz shear acoustic waves generation in materials with significant coupling between magnetic and lattice subsystems.

II. SAMPLES AND EXPERIMENTAL METHODS

Epitaxial thin films composed of a binary cubic C15-Laves alloy $TbFe_2$ have been grown using molecular beam epitaxy. $TbFe_2$ combines large magnetostriction of rare-earth terbium and strong exchange coupling of 3d iron. Such compounds for which the built-in magnetostrictive strain at room temperature lies close to 1% [29], are often known as the most magnetostrictive ferromagnetic compounds to date, even-though, strictly writing, $TbFe_2$ is in fact a ferrimagnet. An asymmetry of the terbium 4f electron cloud is suggested to be the main origin of its strong magnetocrystalline anisotropy [29,30]. The typical sample layout that we have investigated is composed of a single-crystalline terfenol film of 300 nm thickness coated with an amorphous fused silica dielectric layer of about 1100 nm thickness, see Fig. 1(a) and [31] for more technical details on the experiments. Samples were grown on Al_2O_3 (11$\bar{2}$0) single crystal substrates by means of molecular beam epitaxy. Substrates were preliminary out-gazed for several hours at 1070 K, then covered by 500 Å of Nb (110) buffer layer at 1070 K. A single atomic layer of Fe was then deposited on top at 820 K, followed by the deposition of single crystals (110) $TbFe_2$ thin films [32,33]. Ultimately, the metallic multilayer structure was transferred under vacuum to another chamber and coated with a transparent dielectric layer of silica SiO_2, chosen for its well defined mechanical and optical properties at the femtosecond probe laser wavelength [34].

The static magnetic properties of the terfenol films were analyzed by employing a static vibrating-sample magnetometer (VSM) up to 2 Tesla. VSM measurements were performed with an external magnetic field applied either in-plane or at some angle from the sample surface normal, see Figs. 1(b) and 1(c). The shape of the VSM magnetic hysteresis loops in Fig. 1(b), recorded under different directions and strengths of an in-plane magnetic field, indicate an in-plane preferential orientation of the magnetization vector along [$\bar{1}$10] and reveals the magnetocrystalline anisotropy of the films. Figure 1(b) indicates that [001] and [$\bar{1}$10] are the hard and easy axes, respectively. The coercive field along the [$\bar{1}$10] easy

axis lies in the range of 6.5 kOe. Figure 1(c) shows the VSM magnetic hysteresis loops recorded in case of an external magnetic field applied at different angles from the sample normal. As expected from the magnetic shape anisotropy of thin films, the magnetization of the $TbFe_2$ layer lies preferentially in the sample surface. As indicated on Fig. 1(c), in order to significantly tilt the magnetization out-of-plane a magnetic field strength of several teslas is needed.

The ultrafast pump-probe experiments were performed using a 250 kHz regenerative Ti:Sapphire amplified laser system (Coherent RegA) delivering ∼4 μJ optical pulses of 250 fs duration, at a central wavelength of 800 nm. A portion of the laser output, the so-called pump beam, in the range of 0.1–2 μJ, was synchronously modulated in amplitude by an acousto-optic modulator with a square wave function at 50 kHz frequency, a subharmonic frequency of the laser repetition rate. The pump beam was then focused at an oblique incident angle of about 70° from the normal of the magnetic sample surface with a spot size of about ∼100 μm FWHM along the vertical dimension. Upon thermoelastic transient heating, demagnetization and release of magnetostrictive strains, the acoustic waves are laser-excited by the pump beam at the $TbFe_2$ optical skin depth and injected into the surrounding SiO_2 layer, see Fig. 1(a). A ten times less intense time-delayed probe beam at a central wavelength of 800 nm was focused at an oblique incident angle of about 70° from the normal of the sample surface, and overlapped with the pump beam at the sample surface. The probe spot size on the sample surface was about ∼60 μm FWHM along the vertical dimension. In order to monitor the transient laser-induced demagnetization, heating, as well as the acoustic waves propagation in the SiO_2 layer as a function of time delay between pump and probe beams, the portion of the probe beam reflected at the sample was directed to a balanced photodiode coupled to a lock-in amplifier synchronized at the pump modulation frequency. For the specific analysis of transient rotation of the probe polarization, we used a conventional magnetooptical Kerr effect (MOKE) configuration, that consists of the sequential combination of a zero-order half-waveplate, a Wollaston prism and a balanced large area photodetector. The Wollaston prism was used to split the probe beam into two cross-polarized s and p subbeams, each of these two subbeams was directed to a distinct photodiode. The half-waveplate, mounted on a motorized rotation stage, is used to control the light intensity of each subbeam. The proper balanced angle of the half-waveplate that corresponds to equal intensity on both arms of the photodetector, was set by minimizing the output of the balanced photodetector, with an accuracy better than 0.1°. The investigated samples were placed at the center of the "magnetic stargate" holder that can be used to apply a static magnetic field at a strength up to 7.5 kOe, see Fig. 1(d). To note that the so-called "magnetic stargate" holder is composed of a nonmagnetic sample holder placed in the ∼1 cm gap between two magnetic pyramids facing each other. These pyramids of opposite poles are made of a stack of Neodymium magnets attached to a ball bearing stage, such that the direction of the applied magnetic field can be rotated around the sample in pretty much all directions. The maximum magnetic field strength of the "magnetic stargate" is slightly higher than the easy axis coercive field of 6.5 kOe. The "magnetic stargate" was systematically rotated in order to apply the magnetic field along the sample easy axis $[\bar{1}10]$, prior to the ultrafast measurements, to ensure that the initial magnetization state is set along the easy axis. This magnetic strength is however insufficient to fully tilt the magnetization out-of-plane. From Fig. 1(c), at a field strength of 7.5 kOe along [110] [90° in Fig. 1(c)], the magnetization is about 100 emu/cm^3, as compared to the magnetization at saturation of about 790 emu/cm^3, it means that the tilt angle θ is in the range of $\arcsin(100/790) \sim 7°$. This estimate of the tilt angle will be handy for the discussion in the theoretical sections.

III. EXPERIMENTAL RESULTS AND DISCUSSION

Figure 1(e) shows a time-resolved differential MOKE signal obtained after subtraction of data recorded at two opposite out-of-plane magnetic fields $\pm H$. The data subtraction with respect to H allows to filter spurious contribution to the MOKE signal that does not depend on the polarity of the magnetic field. In the following, we will show that shear acoustic waves excited through demagnetostriction change sign when the polarity of the magnetic field is changed. As a matter of fact, magnetostrictive shear strains are not canceled out from subtraction of data obtained at two opposite fields. This counterintuitive effect that could have misguided the data interpretation in Ref. [27], will be clarified in the theoretical section. The differential MOKE response of Fig. 1(e) reveals an ultrafast laser-induced demagnetization event at a time delay close to 0 that last for only few picoseconds (ps), followed by a fast remagnetization process from 10 to 100 ps. To note that the ultrafast demagnetization event seems slower than in case of polycristalline $TbFe_2$ alloy [35]. Since the Kerr rotation angle changes sign from 10 to 100 ps, the measured transient magnetization component flip signs accordingly. At longer time delays, the MOKE data shows a long-lasting decaying magnetization background, starting at about 100 ps, which indicates that the transient magnetization slowly recovers to its equilibrium state after several nanoseconds. The full demagnetization and remagnetization history could be understood considering the fact that the $[\bar{1}10]$ sample easy axis has been oriented, on purpose, orthogonally to the optical plane of incidence in the transverse MOKE geometry. Considering that the transverse MOKE geometry does not entail any rotation of the probe polarization and the fact that the initial magnetization is along the easy axis with a negligible in-plane component along the z axis, we will explain in the following theoretical sections that our oblique MOKE configuration predominantly matches the longitudinal MOKE geometry which is sensitive to the in-plane magnetization vector M_z.

Upon both thermoelastic transient heating and ultrafast release of the magnetostrictive strains, acoustic waves are laser-excited over the optical skin depth of the $TbFe_2$ thin film and subsequently propagate in the attached SiO_2 layer. After a characteristic acoustic time of flight through the SiO_2 layer, these acoustic waves are partially transferred back to the $TbFe_2$ thin film where they induce, through magnetoelastic interaction a transient change of magnetization that can be measured through MOKE. Figure 1(e) reveals several acoustic pulses with longitudinal (L) or supposedly shear (S)

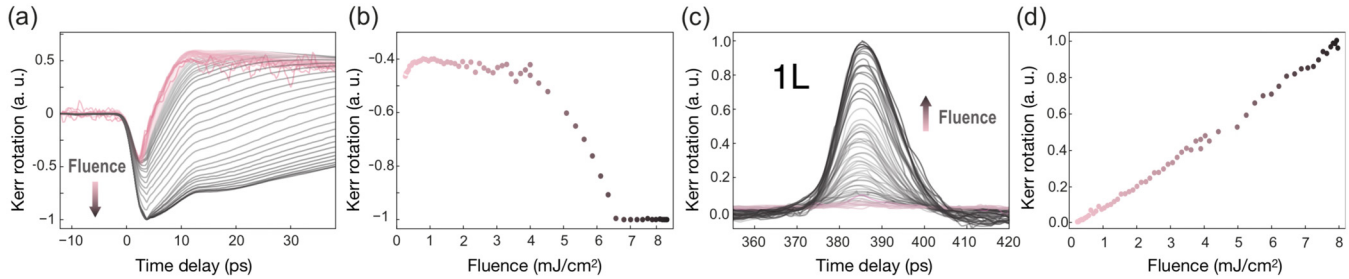

FIG. 2. Time-resolved differential MOKE data as a function of pump fluence obtained under a magnetic field strength of 7.5 kOe. (a) Time and (b) amplitude evolution of the ultrafast laser demagnetization peak. (c) Time and (d) amplitude evolution of the differential MOKE data for the longitudinal acoustic pulse. The thermal background in (c) has been numerically removed for clarity.

acoustic polarizations on top of the remagnetization background. Taking into account the known thickness $d \sim 1100$ nm, longitudinal v_l' and shear v_s' acoustic velocities—of about 5900 and 3700 m s^{-1}, respectively—of the SiO_2 layer [36], the acoustic polarization of these pulses can be inferred. Acoustic pulses on the MOKE signal centered at 383, 754, 1125, and 1497 ps and separated by an acoustic time of flight of $2d/v_l' \simeq 370$ ps are attributed without any ambiguity to the successive longitudinal pulses traveling back and forth in the dielectric layer. These successive longitudinal pulses show alternating change of polarity, which is a result of acoustic reflections at the interfaces that flip the strain sign, and a decrease in amplitude as the result of acoustic attenuation and partial transmission through the sample interfaces. From time of flight considerations, the pulse termed L-S in inset of Fig. 1(e) at about 930 ps can be identified as the reflection of the L pulse into a shear pulse. Due to the complexity of the theory behind this acoustic mode conversion mechanism mediated through magnetostriction, this is out-of-scope of the present manuscript. The data show as well a weak MOKE pulse centered at 180 ps that is a longitudinal acoustic pulse backscattered from the $TbFe_2$/Nb and Nb/Al_2O_3 interfaces. To note that despite the transient demagnetization of the magnetic film, there are no signatures of laser-induced magnetization precession on the MOKE data. We believe that the reason for the absence of precession comes from the fact that the magnetization and the magnetic field are very far-off. Other experiments performed with almost collinear magnetic field and magnetization, not shown here, have evidenced a damped precession at a frequency of about 6 GHz.

Fluence dependent measurements were performed on the same sample to determine the characteristic demagnetization timescale and efficiency, which is a key aspect for the understanding of ultrafast demagnetostriction. Figure 2 presents time- and fluence-resolved differential MOKE data. The MOKE response at a short delay of 3 ps, as shown in Figs. 2(a) and 2(b), indicates that the transient modification of M_z amplitude, does not behave linearly with increasing fluence at all, and resembles closely to the well-known Curie-Weiss law for which the temperature behavior of magnetization follows $M \sim 1/(T - T_c)$, where T_c is the Curie temperature, of 711 K for terfenol [37]. We can probably understand these results as the emergence of maximum possible demagnetization at a characteristic fluence of about $F_c = 6.5$ mJ/cm^2, that drives the $TbFe_2$ spin/electronic temperature close to a characteristic temperature equivalent to the Curie temperature. This interpretation stands only if above F_c the constant Kerr rotation angle in Fig. 2(b) reflects laser demagnetization of the sample, otherwise, it might be related to temperature dependent magnetization alignement under a rather strong external magnetic field. The fluence dependence of the sign flip around 10 ps at low fluences, that gets shifted to much longer times at high fluences, might evidence as well the vicinity of the Curie temperature during laser-induced demagnetization [38,39]. Modeling this demagnetization behavior is in fact rather complex and still an open question for more than three decades [8,40]. This is out-of-scope of the present paper.

At the contrary to the demagnetization pulse, the fluence dependence of the MOKE signal at 385 ps, that corresponds to the first longitudinal acoustic pulse, evolves almost perfectly linearly with increasing laser fluence, see Figs. 2(c) and 2(d). It is important to be cautious about the fact that this MOKE signal is a convolution of the laser-generation process with the laser-detection process of strain acoustic waves. As for the detection process, since, unlike shear acoustic waves, longitudinal acoustic waves do not induce any rotation of the probe polarization [26], these MOKE data for longitudinal pulses can only come from inverse magnetoelastic interactions. In fact, if we neglect spurious detection mechanisms that could be prevalent in weakly magnetostrictive compounds [14], which is supposedly not the case for terfenol which is by far the most magnetostrictive compound, the longitudinal acoustic waves shake the magnetization through inverse magnetostriction, and create a transient δM_z component that is detected through MOKE. This detection mechanism is linear with the strain amplitude, see Ref. [16] and theoretical Sec. IV. As for the generation process, if we consider the thermoelastic mechanism which is most often the predominant mechanism for laser-excitation of strain waves in case of metals, in this case, the acoustic strain amplitude should follow a linear relationship with laser fluence [24]. We can then conclude that the MOKE fluence dependent measurements of the longitudinal acoustic pulse establish that the laser-excitation mechanism is predominantly thermoelastic. At first glance, there is no demagnetostriction effect for the laser excitation of longitudinal acoustic waves. However, if we look closely to the curve displayed in Fig. 2(d), in the fluence range from 4 to 6.5 mJ/cm^2 where the MOKE demagnetization amplitude evolves significantly, it seems that the linear evolution of the MOKE signal becomes irregular. This irregularity of the linear behavior at high fluence might be simply an experimental

artifact or it could come from demagnetostriction, which is a complex mechanism whose theoretical basis will be discussed in the theoretical section.

The inset of Fig. 1(e) highlights on the MOKE data a transient pulse centered at a time delay of 551 ps. If we take into account the uncertainties on the SiO_2 thickness, as well as the discrepancies on the longitudinal and shear acoustic velocities found in the literature [36], this time delay matches fairly well the acoustic time-of-flight of shear acoustic pulses across the SiO_2 layer of $2d/v_s' \simeq 594$ ps. We recall that the only possible mechanism for shear acoustic excitation in this high-symmetry magnetic sample is demagnetostriction. Due to symmetry considerations, the thermoelastic mechanism cannot excite shear acoustic waves that require broken symmetry to get efficiently laser-excited [26]. Occasionally, under a variety of experimental circumstances, demagnetostriction can break the symmetry required to laser-excite shear waves. The maximum strain amplitude that could be released by laser-demagnetization of the sample is limited by the magnetostriction constant. In case of terfenol, this constant can reach an enormous value of 10^{-2} [29], which is most often higher than the strain level typically excited in metallic samples through the thermoelastic effect [21]. However, as compared to the L pulse, the detected S-pulse amplitude in Fig. 1(e) is unsatisfying. Either the weakness of the S pulse comes from a rather inefficient excitation mechanism, either from a rather weak detection mechanism. We recall that shear acoustic waves do rotate the probe polarization and produce a Kerr signal even in a nonmagnetic sample. In order not to confuse the readers, the shear detection is most often referred as depolarized Brillouin scattering, rather than MOKE [26], even if both techniques are technically based on the detection of the rotation of the probe polarization. In case of shear acoustic waves detection, magnetooptic coefficients are of course irrelevant, and it is only the photoelastic coefficients involving shear strains that matter. Therefore the weakness of the detected S pulse could come from a tiny photoelastic coefficient of terfenol at the probe wavelength but it could simply come from the fact that the demagnetostriction is not optimum. As we will see in the next theoretical section, the efficiency of the demagnetostriction mechanism could be experimentally optimized further. Unfortunately, this would require stronger magnetic fields that were not available at the moment when the experiments were performed.

The weakness of the S pulse, slightly above the noise level, can question the authenticity of the shear nature of this acoustic pulse. In fact, there are several indications, in addition to the estimate on the time-of-flight of this acoustic pulse, that tend to justify our interpretation. For instance, time-resolved x-ray diffraction measurements have shown that this S pulse does not clearly shows up on the diffraction data, at the contrary to the L pulses, see Fig. 4(a) in Ref. [21]. We have performed as well experiments with a terfenol sample with a much thicker SiO_2 cover layer, at a probe wavelength of 400 nm for which the Brillouin scattering signal is known to be rather efficient. Figure 3 shows the recorded time-resolved depolarized Brillouin data that highlights two frequencies that match the longitudinal and shear Brillouin frequencies of SiO_2, see Ref. [26]. The presence of a Brillouin frequency close to 22 GHz, even of rather weak amplitude, demonstrates

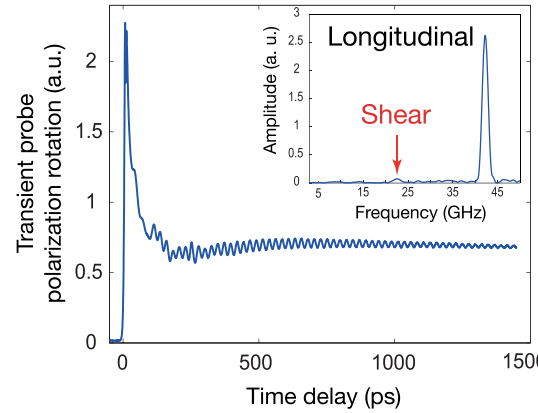

FIG. 3. Time-resolved depolarized Brillouin scattering signal recorded for a similar terfenol sample with much thicker SiO_2 cover layer. The frequency spectrum shown in inset reveals light-scattering at a 400 nm probe wavelength from longitudinal and shear coherent acoustic waves at the expected Brillouin frequencies of SiO_2.

the propagation of shear acoustic strains in the SiO_2 cover layer and asserts the laser-induced demagnetostriction mechanism for the excitation of shear acoustic waves. To go beyond these proof-of-concept experimental results, we will discuss in the following the theoretical basis of ultrafast demagnetostriction.

IV. ANALYTICAL MODEL FOR DEMAGNETOSTRICTION

A. Static magnetostrictive strains

Let us derive the analytical expressions of the static built-in strains in the terfenol thin film. Figure 4 depicts the considered sample geometry and coordinate axes for the theoretical analysis. Since the terfenol film thickness is much greater than the optical skin depth, and the laser spot size is much greater than the film thickness, we will consider two semi-infinite media made of $TbFe_2$ and SiO_2 for modeling the local laser excitation process. There are three possible strains propagating along any specific direction in a solid, a longitudinal or quasi-longitudinal acoustic wave and two shear acoustic waves. In

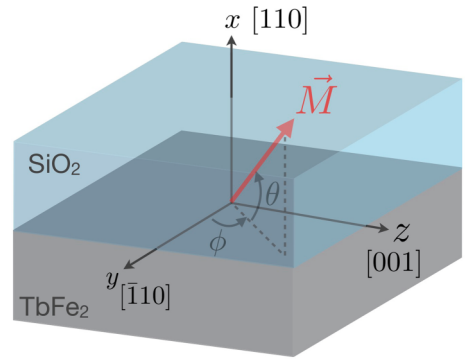

FIG. 4. For the analytical modeling, the sample is composed of a semi-infinite (110) monocrystalline magnetic $TbFe_2$ medium, with arbitrary direction of magnetization $\vec{M}$, and a semi-infinite transparent dielectric SiO_2 medium. The laser excitation and detection takes place within the optical penetration depth in the $TbFe_2$ medium.

the considered sample geometry of Fig. 1(a), these strains propagating along the out-of-plane x-axis have the tensorial form ε_{xx} for longitudinal, and ε_{xy}, ε_{xz} for shear. We recall that strains are displacements gradients. Since the sample is assumed infinite in the y and z directions, the spatial derivatives over y and z are zero and so for the longitudinal strains ε_{yy}, ε_{zz}, and the shear strain ε_{yz},

$$\varepsilon_{yy} = \varepsilon_{zz} = \varepsilon_{yz} = 0. \tag{1}$$

Built-in static magnetostrictive strains in magnetic materials are derived by minimizing the free energy density

$$F_{_T} = F_k + F_e + F_z + F_{\text{ex}}, \tag{2}$$

where F_k, F_e, F_z, and F_{ex} are the magnetocrystalline anisotropy, elastic, Zeeman and exchange energies respectively. In case of ferromagnetic materials, some contributions can be omitted: dipole-dipole energy is much lower than exchange energy. Exchange coupling between terbium and iron moments is about 300 T [41], so we can presume that the magnetic moments always keep their original ferromagnetic configuration. The terfenol film thickness is assumed to be large enough (hundreds of nm) to exhibit spherical symmetry, hence surface effects can be neglected as well. The expression of the magnetocrystalline anisotropy energy F_k can be expanded using Taylor series in strains, in the form [42]

$$F_k(m_i, \varepsilon_{ij}) = F_a(m_i) + F_{\text{me}}(m, \varepsilon_{ij}), \tag{3}$$

where F_a is the anisotropy energy, F_{me} the magnetoelastic energy, m_i the cosines direction of the unit vector $\vec{m}$ that matches the direction of magnetization $\vec{M}$, and ε_{ij} the strain tensor. To note that, in case of terfenol of cubic symmetry, the anisotropy energy written in the [100], [010], [001] coordinates reads

$$F_a = K_1\left(m_x^2 m_y^2 + m_y^2 m_z^2 + m_x^2 m_z^2\right), \tag{4}$$

where $K_1 = -760\times10^{-4}$ Pa is the anisotropy constant for $TbFe_2$ [29]. Among all these energy terms in Eqs. (2) and (3), only two are linked with strains and are relevant for our analysis, the magnetoelastic energy term F_{me} and the elastic energy term F_e.

Cumbersome calculations of the elastic energy F_e written in the (x, y, z) coordinate system, detailed in Appendix A, lead to

$$F_e = \frac{1}{2}\left[\left(\frac{c_{11}+c_{12}}{2} + c_{44}\right)\varepsilon_{xx}^2 + 2(c_{11}-c_{12})\,\varepsilon_{xy}^2 + 4\,c_{44}\,\varepsilon_{xz}^2\right], \tag{5}$$

where c_{11}, c_{12}, and c_{44} are the elastic constants of terfenol. These constants are unknown, however, since $Tb_{0.3}Dy_{0.7}Fe_2$ (terfenol-D) possesses similar lattice parameters, its elastic constants are most probably similar to the values $c_{11} = 14.1\times10^{10}$ N/m^2, $c_{12} = 6.48\times10^{10}$ N/m^2, and $c_{44} = 4.87\times10^{10}$ N/m^2 of terfenol-D [43]. Unlike magnetoelastic energy, the elastic energy is independent on the magnetization. It introduces a positive contribution to the total free energy density.

After some intricate tensorial calculations, detailed in Appendix A, the magnetoelastic energy expressed in the coordinate system (x, y, z) takes the form,

$$F_{\text{me}} = b_1\left(\frac{1}{2}\left(m_x^2 + m_y^2\right)\varepsilon_{xx} + 4m_x m_y \varepsilon_{xy}\right) + b_2\left(\frac{1}{8}\left(m_x^2 - m_y^2\right)\varepsilon_{xx} + m_x m_z \varepsilon_{xz}\right). \tag{6}$$

Note that the magnetoelastic constants b_1 and b_2 are linked to the magnetostrictive constants $\lambda_{[100]}$ and $\lambda_{[111]}$ through the following relationship [44]:

$$\lambda_{[100]} = \frac{-2\,b_1}{3(c_{11}-c_{12})}, \qquad \lambda_{[111]} = \frac{-b_2}{3\,c_{44}}. \tag{7}$$

These magnetostrictive constants $\lambda_{[100]}$ and $\lambda_{[111]}$ are the strains experimentally measured in the [100] and [111] crystallographic directions of the magnetostrictive samples. $TbFe_2$ exhibits a strong magnetoelastic anisotropy with $\lambda_{[100]} = 300\times10^{-6}$ and $\lambda_{[111]} = 2460\times10^{-6}$ [29]. From the elastic constants in Ref. [43], we can calculate the magnetoelastic constants of terfenol, $b_2 = -359.4$ MPa and $b_1 = -34.3$ MPa $\ll b_2$.

The expressions of the static built-in strains of [110] terfenol crystals of arbitrary direction of magnetization can now be calculated by searching extrema in energy in the form

$$\frac{\partial F_{_T}}{\partial \varepsilon_{xx}} = 0, \quad \frac{\partial F_{_T}}{\partial \varepsilon_{xy}} = 0, \quad \frac{\partial F_{_T}}{\partial \varepsilon_{xz}} = 0, \tag{8}$$

where the total energy density $F_{_T}$ can be reduced to only the summation of $F_e + F_{\text{me}}$, which are the only energy terms that are linked to the strains. After summation and derivation of Eqs. (5) and (6), we obtain the expressions of the built-in strains

$$\varepsilon_{xx} = -\frac{b_1\left(m_x^2 + m_y^2\right) + b_2/4\left(m_x^2 - m_y^2\right)}{c_{11} + c_{12} + 2c_{44}}, \tag{9}$$

$$\varepsilon_{xy} = -\frac{2b_1(m_x m_y)}{c_{11} - c_{12}}, \tag{10}$$

$$\varepsilon_{xz} = -\frac{b_2(m_x m_z)}{4c_{44}}, \tag{11}$$

where ε_{xx} is the longitudinal and ε_{xy}, ε_{xz} are the shear static strains.

The coupled formulas (9)–(11) that link the strains and the magnetization vector are extremely insightful for the understanding of the interplay between magnetization and lattice distortion. When the magnetization vector changes direction or amplitude, it releases strains with longitudinal and shear acoustic polarizations. From these formulas, it appears that these magnetoelastic strains can happen to be zero if the magnetization vector points fully on the z direction for the longitudinal strain and either fully along any of the x, y, or z directions for the shear strains. In case of shear strains, these nodes correspond to crystallographic directions of high symmetry for which the symmetry is not broken. As a matter of fact, shear strains appear from lattice symmetry breaking [26], which can be accomplished from a mechanism such as magnetostriction that intrinsically breaks the symmetry. As

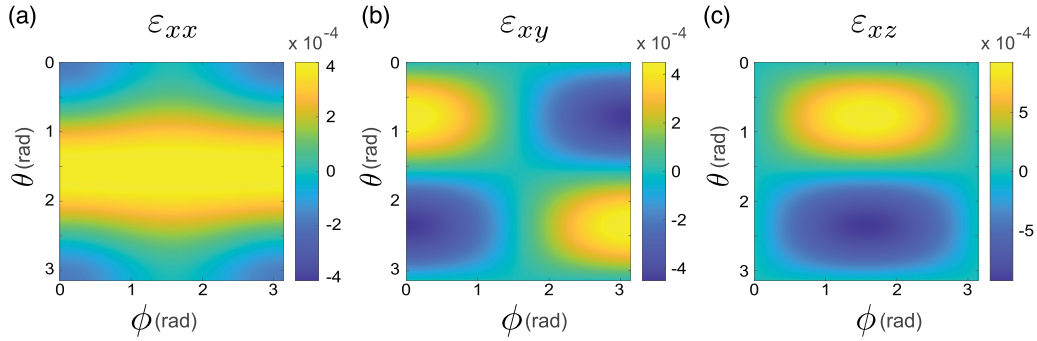

FIG. 5. Numerical simulations of the angular dependence of the longitudinal (a) ε_{xx} and the shear (b) ε_{xy}, (c) ε_{xz} static strain amplitudes at various magnetization orientations defined by θ and ϕ, the out-of-plane tilt and azimuthal angles of $\vec{M}$ respectively.

shown in Fig. 5 that displays the numerical simulations of the terfenol static built-in strains of Eq. (10) and (11), the shear strain amplitudes reach a maxima at an optimum tilt angle θ of 0.78 rad or 1.57 rad at ϕ =0. From Eq. (7) and as pointed out on Fig. 5, the shear strain ε_{xz} can reach at most an amplitude of $3/8\lambda_{[111]} = 9.2\times10^{-4}$, about twice higher than the shear strain ε_{xy} that can at most reach an amplitude of $3/2\lambda_{[100]} = 4.5\times10^{-4}$. To note that according to Eqs. (10) and (11), the shear built-in strains change sign if the static out-of-plane magnetization changes sign. Therefore, upon the application of an external out-of-plane magnetic field at $\pm H$, the static shear strains change sign accordingly.

In case of a cubic (100) ferromagnet, as, for example, in Ref. [27], the shear strains easily calculated from Eqs. (A2)–(A14) read

$$\varepsilon^*_{xy} = -\frac{b_2(m^*_x m^*_y)}{8c_{44}}, \quad \varepsilon^*_{xz} = -\frac{b_2(m^*_x m^*_z)}{8c_{44}}. \tag{12}$$

The magnetostrictive shear strains reverse sign as well if the out-of-plane magnetization changes sign. The fact that magnetostrictive shear strains change sign at ±H is a rather general trend that has been unfortunately discarded in Ref. [27]. See Appendix B for calculation and discussion of the strains in case of a (111) magnetostrictive sample.

Overall, since laser-mediated release of static built-in strains launches propagative acoustic waves, these analytical results are of primarily importance for the optimization of acoustic excitation that coincides with maximization of the built-in magnetostrictive strains. In particular, we can conclude that the maximum shear excitation corresponds to a tilted magnetization vector, ideally at an angle $\theta = 45^\circ \equiv 0.78$ rad out-of-plane at the optimum ϕ angle. Experimentally, from the VSM curves displayed in Fig. 1(c), such tilt angle would require a magnetic field twice higher than what can currently provide the "magnetic stargate." At this optimum tilt angle, the built-in shear strains would be about about six times stronger as compared to a tilt angle of 7°.

B. MOKE detection of acoustic waves, the inverse magnetostrictive effect

The coupled formulas (9)–(11) gather crucial informations on the built-in magnetostrictive strains but not on the converse effect, the magnetization modification induced by longitudinal or shear strains. Indeed, these equations are linked to the equilibrium condition of the lattice and cannot be used to track the equilibrium condition of magnetization at all. Let us briefly discuss the inverse magnetostrictive effect that translates experimentally into the MOKE detection of ultrafast acoustic strains via magnetoelastic interactions, in a similar manner than the experimental results described in the previous section. In order to analytically solve the inverse magnetostriction effect, the starting point is the Landau-Lifshitz equation that can predict the change of magnetization in response to an acoustic perturbation [13–16]. The Landau-Lifshitz equation has the general form,

$$\frac{\partial \vec{m}}{\partial t} = -\gamma\mu_0 \vec{m} \times \vec{H}_{\text{eff}}, \tag{13}$$

where γ, μ_0, and $\vec{H}_{\text{eff}}$ are the gyromagnetic ratio, the magnetic permeability of vacuum, and the effective magnetic field respectively. Note that the damping term in the Landau-Lifshitz equation has been omitted for simplicity. The set of equations can be expanded in the coordinate axes x, y, and z as

$$\begin{aligned}
\frac{\partial m_x}{\partial t} &= -\gamma\mu_0(m_y H_{\text{eff},z} - m_z H_{\text{eff},y}),\\
\frac{\partial m_y}{\partial t} &= -\gamma\mu_0(m_z H_{\text{eff},x} - m_x H_{\text{eff},z}),\\
\frac{\partial m_z}{\partial t} &= -\gamma\mu_0(m_x H_{\text{eff},y} - m_y H_{\text{eff},x}).
\end{aligned} \tag{14}$$

The projection of the effective magnetic field $\vec{H}_{\text{eff}}$ on the x, y, and z coordinate axes are defined as

$$H_{\text{eff},i} = -\frac{1}{\mu_0 M_0}\frac{\partial F_T}{\partial m_i}, \tag{15}$$

where M_0 is the saturation of magnetization and F_T is the free energy density of Eq. (2). The Landau-Lifshitz equation expresses the fact that a perturbation of the free energy density linked to the magnetization vector, causes the appearance of an effective magnetic field $\vec{H}_{\text{eff}}$ that drives the magnetization vector into a new static or transient equilibrium point of magnetization for which the effective magnetic field and the magnetization vector are collinear.

The effective magnetic field can be decomposed into a static term, that defines the static equilibrium point of the magnetization vector, and a dynamic term that is linked to the

transient perturbation of the free energy due to the acoustic strain through the magnetoelastic free energy term, see Supplemental in Ref. [16]. The effective magnetic field that gives rise to a transient magnetization vector in Eq. (13) can then be reduced to the following transient magnetic field,

$$H_{\mathrm{eff},i(t)} = -\frac{1}{\mu_0 M_0}\frac{\partial F_{\mathrm{me}(t)}}{\partial m_i}. \tag{16}$$

After derivation of the magnetoelastic free energy F_{me} of Eq. (6), the transient magnetic field can be decomposed into

$$\begin{aligned}
H_{\mathrm{eff},x} &= \frac{-1}{\mu_0 M_0}\left[\left(b_1+\frac{b_2}{4}\right)m_x\varepsilon_{xx} + 4b_1 m_y\varepsilon_{xy} + b_2 m_z\varepsilon_{xz}\right],\\
H_{\mathrm{eff},y} &= \frac{-1}{\mu_0 M_0}\left[\left(b_1-\frac{b_2}{4}\right)m_y\varepsilon_{xx} + 4b_1 m_x\varepsilon_{xy}\right],\\
H_{\mathrm{eff},z} &= \frac{-1}{\mu_0 M_0}[b_2 m_x\varepsilon_{zx}].
\end{aligned} \tag{17}$$

We can then calculate the transient change of magnetization of Eq. (14) that reads

$$\begin{aligned}
\frac{\partial m_x}{\partial t} &= \frac{\gamma}{M_0}\left[-\left(b_1-\frac{b_2}{4}\right)m_y m_z\varepsilon_{xx} - 4b_1 m_x m_z\varepsilon_{xy}\right.\\
&\qquad \left. + b_2 m_x m_y\varepsilon_{xz}\right],
\end{aligned} \tag{18}$$

$$\begin{aligned}
\frac{\partial m_y}{\partial t} &= \frac{\gamma}{M_0}\left[\left(b_1+\frac{b_2}{4}\right)m_x m_z\varepsilon_{xx} + 4b_1 m_y m_z\varepsilon_{xy}\right.\\
&\qquad \left. - b_2\left(m_x^2 - m_z^2\right)\varepsilon_{xz}\right],
\end{aligned} \tag{19}$$

$$\begin{aligned}
\frac{\partial m_z}{\partial t} &= \frac{\gamma}{M_0}\left[-\frac{b_2}{2}m_x m_y\varepsilon_{xx} + 4b_1\left(m_x^2 - m_y^2\right)\varepsilon_{xy}\right.\\
&\qquad \left. - b_2 m_y m_z\varepsilon_{xz}\right].
\end{aligned} \tag{20}$$

This set of equations highlight the effect of a perturbative longitudinal ε_{xx} or shear ε_{xy} and ε_{xz} acoustic strains that give rise to δm_x, δm_y, and δm_z magnetization components. Experimentally, according to our experimental geometry depicted in Fig. 1(d), δm_x can be measured through transient polar MOKE, δm_z through transient longitudinal MOKE and δm_y through transverse MOKE. Since transverse MOKE, at the contrary to longitudinal and polar MOKE, has no effect on the polarization, it induces a change of reflectivity only, it is irrelevant to our experimental scheme. Let us consider only the two measurable components δm_x and δm_z from now on.

As stated previously, the static magnetization predominantly lies along the magnetic easy axis in the y direction, giving $m_y \sim 1$ and $m_z \sim 0$. From Eq. (18), it means that polar MOKE is not sensitive to longitudinal acoustic strains in such configuration. At the contrary, from Eq. (20), longitudinal MOKE is sensitive to longitudinal strains at the condition that $m_x \neq 0$. Technically, it means that the efficient longitudinal MOKE detection of longitudinal strains requires the application of an out-of-plane magnetic field H in order to tilt the static magnetization out-of-plane and to create a nonzero m_x. To note that since m_x changes sign with H, the differential longitudinal MOKE obtained after subtraction of two longitudinal MOKE data recorded at two opposite out-of-plane magnetic fields $\pm$H, does not cancel the detection of longitudinal strains.

In case of shear strains, the detection and the excitation are coupled together. For instance, with the condition that the static magnetization lies mainly along the easy axis of magnetization m_y, that implies in fact that the shear acoustic strain of Eq. (11) vanishes, i.e., $\varepsilon_{xz} \sim 0$ since $m_z \sim 0$, then, only the longitudinal MOKE of Eq. (20) is sensitive to shear acoustic strains ε_{xy}. All in all, the polar MOKE does not couple to shear acoustic strains, which are either not excited or not detected. Only the longitudinal MOKE of Eq. (20) is sensitive to shear acoustic strains ε_{xy}. To note that since the longitudinal MOKE detection of the only nonzero shear acoustic strain ε_{xy} in Eq. (20) is weighted by a quadratic term m_x^2, the differential longitudinal MOKE of these shear strains should vanish. However, since the shear strain changes sign when the out-of-plane magnetization m_x is flipped upon reversal of the external magnetic field H, see Eq. (10), the differential longitudinal MOKE is not canceled if we consider the shear excitation and the shear detection all together.

To summarize the MOKE detection in our experimental conditions, it is mainly the longitudinal MOKE that can efficiently detect longitudinal ε_{xx} and shear ε_{xy} acoustic strains. However, we recall that shear acoustic waves polarized along the y axis, such as shear acoustic strains ε_{xy}, can be detected in a nonmagnetic medium from the photoelastic effect, see Ref. [26]. Shear waves acoustically polarized vertically to the optical plane of incidence entail a rotation of the probe polarization from the photoelastic effect that can be detected through a conventional depolarized setup, composed of a half-waveplate, a wollaston, and a balanced photodectector. This detection scheme is strictly identical to a MOKE setup sensitive to the rotation of the probe polarization. This is quite different for longitudinal acoustic waves that can only induce birefringence without almost any effect on the rotation of the (main axis) of the probe polarization [45]. As a matter of fact longitudinal acoustic waves do not tilt the probe polarization, at the contrary to shear acoustic waves. Therefore both longitudinal MOKE and photoelastic effects, can be involved during the detection process of shear acoustic strains ε_{xy}, which might favor or not the overall detection sensitivity. Since the photoelastic and magnetooptic coefficients of terfenol are unknown, it is difficult to judge on the effectiveness of the shear detection of shear acoustic strains ε_{xy} in our experiment.

C. Lattice dynamics

In order to analytically resolve the ultrafast laser-mediated release of the built-in magnetostrictive strains and the excitation of acoustic strains transmitted in the dielectric medium, for the sample geometry depicted in Figs. 1(a) and 4, it is required to solve the coupled Newton's second law, which in case of continuous media can be written as

$$\begin{aligned}
\rho\frac{\partial^2 u_i}{\partial t^2} &= \frac{\partial \sigma_{ij}}{\partial x_j},\\
\rho'\frac{\partial^2 u_i'}{\partial t^2} &= \frac{\partial \sigma_{ij}'}{\partial x_j},
\end{aligned} \tag{21}$$

where $u_i^{(\prime)}$ denotes the acoustic displacement or polarization vector, $\rho^{(\prime)}$ the mass density and $\sigma_{ij}^{(\prime)}$ the stress tensor of the magnetostrictive or dielectric media, the latter being labeled with the superscript $'$. We only consider the propagation of plane acoustic wave along the out-of-plane x direction, consequently, all partial derivatives associated with the propagation along y and z can be omitted and only the terms where $j = x$ in Eq. (21) remain

$$\rho^{(\prime)} \frac{\partial^2 u_i^{(\prime)}}{\partial t^2} = \frac{\partial \sigma_{ix}^{(\prime)}}{\partial x}, \tag{22}$$

where $\sigma_{ix}^{(\prime)}$ are the components of the elastic stress tensor in the coordinate axes ($i = x, y, z$). The general expression of the stress tensor of the magnetostrictive medium is given by

$$\begin{aligned}\sigma_{ij} &= \frac{1+\delta_{ij}}{2}\frac{\partial F_T}{\partial \varepsilon_{ij}} - c_{ijkl}\beta_{kl}T \\ &= \frac{1+\delta_{ij}}{2}\frac{\partial (F_e + F_{\text{me}})}{\partial \varepsilon_{ij}} - c_{ijkl}\beta_{kl}T,\end{aligned} \tag{23}$$

where the total energy density F_T in Eq. (23) can be reduced to the summation of the elastic energy F_e with the magnetoelastic energy F_{me}, that are the only energy terms that depend on the strain, c_{ijkl} is the elastic tensor, β_{kl} the thermal dilatation tensor and T the laser-induced temperature rise. Ultrafast laser-heating of the magnetostrictive material induces a thermoelastic stress $B_{ij}T = c_{ijkl}\beta_{kl}T$ on the right side of Eq. (23) that gives rise to thermal expansion. At the picosecond timescale for which the excitation of the strains takes place, thermal diffusion can most of the time be neglected in the absorbing medium itself and even more in the dielectric material with a much lower thermal diffusion rate. Therefore, from Eq. (A2), the general expression of the stresses in the dielectric medium only contains the elastic term,

$$\sigma'_{ij} = c'_{ijkl}\varepsilon'_{kl}. \tag{24}$$

From Eq. (A2), we can rewrite as well the stresses in the magnetostrictive medium in the form,

$$\begin{aligned}\sigma_{ij} &= c_{ijkl}\varepsilon_{kl} + \frac{1+\delta_{ij}}{2}\frac{\partial F_{\text{me}}}{\partial \varepsilon_{ij}} - c_{ijkl}\beta_{kl}T, \\ &= c_{ijkl}\varepsilon_{kl} + \sigma_{ij}^T,\end{aligned} \tag{25}$$

The right-hand-side term σ_{ij}^T in Eq. (25) denotes the stress source driven by the laser, it comprises two contributions: (i) laser-induced modification of the magnetoelastic energy density and (ii) laser-induced thermoelastic stress. After calculation of the derivation of Eq. (6) over the strain ε_{ij}, the source stresses of Eq. (25) can be expanded as

$$\begin{aligned}\sigma_{xx}^T &= \partial \frac{F_{\text{me}}}{\partial \varepsilon_{xx}} - B_{11}T \\ &= \frac{b_1}{2}\left(m_x^2 + m_y^2\right) + \frac{b_2}{8}\left(m_x^2 - m_y^2\right) - c_{11}\beta_{11}T, \\ \sigma_{xy}^T &= \frac{1}{2}\partial \frac{F_{\text{me}}}{\partial \varepsilon_{xy}} - 0 = 4b_1 m_x m_y, \\ \sigma_{xz}^T &= \frac{1}{2}\partial \frac{F_{\text{me}}}{\partial \varepsilon_{xz}} - 0 = b_2 m_x m_z.\end{aligned} \tag{26}$$

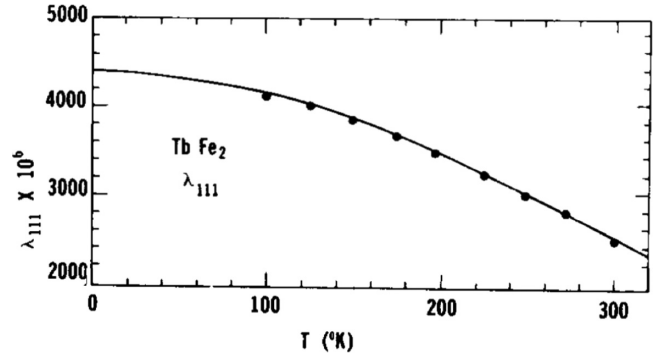

FIG. 6. Temperature evolution of the magnetostriction coefficient $\lambda_{[111]} = -b_2/3c_{44}$. Adapted from Ref. [37].

It is important to notice that in the set of Eq. (26), due to symmetry reasons, only longitudinal stresses σ_{xx} comprise a thermoelastic contribution $c_{11}\beta_{11}T$. On the contrary, shear stresses σ_{xy} and σ_{xz} that do not comprise any thermoelastic contribution can only be excited from demagnetostriction.

At this stage of the analysis, we can already transpose the results detailed in Ref. [46], where the mathematical analysis to solve the thermoelastic laser-excitation in anisotropic media is fully described, to our current model. Shortly, the analytical solutions of the t-Fourier transformed surface displacements transmitted in the dielectric medium can be obtained after solving the full set of equations contained in Eq. (22) and taking into account the continuity of the stresses and displacements at the boundary between the magnetostrictive and dielectric media. The solutions adapted from Ref. [46], can be written in the general form

$$\widetilde{u}_i'(x,\omega) = (-1)^i\, \Gamma_{\text{im}} \widehat{\sigma}_{\text{im}}^T(-jk_m,\omega) e^{jk_i' x}, \tag{27}$$

where the only nonzero Γ_{im} coefficients are

$$\begin{aligned}\Gamma_{xx} &= \left(\rho \upsilon_l^2 + \rho' \upsilon_l \upsilon_l'\right)^{-1}, \\ \Gamma_{xy} &= \left(\rho \upsilon_{t1}^2 + \rho' \upsilon_{t1} \upsilon_t'\right)^{-1}, \\ \Gamma_{xz} &= \left(\rho \upsilon_{t2}^2 + \rho' \upsilon_{t2} \upsilon_t'\right)^{-1},\end{aligned} \tag{28}$$

with υ_l, υ_l', υ_{t1}, υ_{t2}, υ_{t1}', and υ_{t2}' the longitudinal and shear velocities in the two media, k_i' the acoustic wave vectors of the dielectric media, ω the angular frequency, and $\widehat{\sigma}_{\text{im}}^T$ the t-Fourier x-Laplace transform of the stress source of Eq. (26). To proceed further, it is required to model the laser-induced demagnetostriction effect itself in order to calculate $\widehat{\sigma}_{\text{im}}^T$ of Eq. (27). For simplicity, we will assume that the laser-induced demagnetization only decreases the magnetization modulus of the magnetostrictive medium, but not its orientation. Therefore the magnetization direction vectors m_x, m_y, m_z in the set of Eq. (26) remain untouched. In this case, the laser-induced temperature rise alters the magnetoelastic coefficients b_1 or b_2 that decrease with temperature. Once the temperature reaches the Curie temperature of the magnetic material and beyond, these magnetoelastic coefficients become obviously zero. Since the temperature evolution of the magnetostrictive coefficient $\lambda_{[111]} = -b_2/3c_{44}$ shown in Fig. 6 varies linearly with temperature in a temperature range of 100–300 K, and taking into account the negligible temperature modification of

c_{44} in case of iron [47], we will assume in the following a linear relationship in the form

$$b_i = b_{i0} - A_i T, \tag{29}$$

where A_i could be termed the thermo-magneto-elastic coefficients with $i = 1, 2$, that link the magnetoelastic coefficients b_i with the temperature increase T due to ultrafast laser-heating. Note that this linear assumption is aimed to simplify the analysis, that could be transposed to more complex temperature evolution of the magnetoelastic coefficients without excessive difficulties. Under this linear assumption, and neglecting the effect of thermal diffusion, it becomes straightforward to extract the solutions of the strains transmitted and propagating in the dielectric medium, already calculated in [46], we obtain for $t - \frac{x}{v'_{l,t}} > 0$,

$$\varepsilon'_{xx}(x,t) = -\left(\frac{\alpha F}{\rho c_p}\right)\frac{v_l}{v'_l}\Gamma_{xx}\gamma_1\, e^{-\alpha v_l\left(t-\frac{x}{v'_l}\right)}, \tag{30}$$

$$\varepsilon'_{xy}(x,t) = -\left(\frac{\alpha F}{\rho c_p}\right)\frac{v_{t1}}{v'_t}\Gamma_{xy}\gamma_2\, e^{-\alpha v_{t1}\left(t-\frac{x}{v'_t}\right)}, \tag{31}$$

$$\varepsilon'_{xz}(x,t) = -\left(\frac{\alpha F}{\rho c_p}\right)\frac{v_{t2}}{v'_t}\Gamma_{xz}\gamma_3\, e^{-\alpha v_{t2}\left(t-\frac{x}{v'_t}\right)}, \tag{32}$$

where F is the portion of the laser fluence absorbed by the magnetostrictive medium, α the optical absorption coefficient at the given pump wavelength, c_p the specific heat capacity and ρ the density of the magnetic medium. The strains are zero for $t - \frac{x}{v'_{l,t}} < 0$. Note that in the specific case of $TbFe_2$ which is almost elastically isotropic $v_{t1} \simeq v_{t2}$. The γ_i coefficients are defined by

$$\gamma_1 = \frac{A_1}{2}\left(m_x^2 + m_y^2\right) + \frac{A_2}{8}\left(m_x^2 - m_y^2\right) + [c_{11}\beta_{11}], \tag{33}$$

$$\gamma_2 = 4A_1 m_x m_y, \tag{34}$$

$$\gamma_3 = A_2 m_x m_z. \tag{35}$$

The set of Eqs. (30)–(32) gather the expressions of the longitudinal and shear strains laser-excited in the magnetostrictive medium, transmitted and propagating in the dielectric medium. The term $(\alpha F)/(\rho c_p)\Gamma_{\text{im}}\gamma_i$ represents the strain amplitude laser-excited in the terfenol optical skin depth, while the exponent describes the strain propagation in the dielectric medium at the acoustic velocity v_l or v_t. The v_i/v'_i term denotes the shrinking or broadening of the strain profile upon transmission across the two media of different acoustic velocities $v_i \neq v'_i$. As expected, since the only direct mechanism for shear excitation in magnetostrictive films is demagnetostriction, the thermoelastic contribution is absent in case of γ_2 and γ_3. From Eq. (33), the ratio of $A_1/2c_{11}\beta_{11}$ and $A_2/8c_{11}\beta_{11}$ can be calculated to compare the efficiency of the demagnetostriction mechanism with respect to the thermoelastic mechanism. This trivial calculation gives -0.08 and -0.23 respectively, see the parameters used for the calculation listed in Table I. It means that the longitudinal strain excited thought the thermoelastic mechanism, that is by far the predominant mechanism of excitation in all sort of materials and in particular metals, can be weakened from the superposition of the demagnetostriction mechanism in this specific ferromagnetic material exhibiting giant magnetostriction.

TABLE I. Optical, thermal, mechanical and magnetoelastic parameters used in the numerical simulations.

terfenol $TbFe_2$ [29,48,49]	Value
Optical absorption coefficient α, m^{-1}	5.26×10^7
Density ρ, kg/m^3	9170
Specific heat capacity c_p, J/kg.K	350
Thermal dilatation coefficient $\beta \equiv \beta_{11}$, K^{-1}	1.18×10^{-5}
Elastic constant c_{11}, N/m^2	117×10^9
Longitudinal acoustic velocity, v_l, m/s	3572
Shear acoustic velocity, $v_{t1} \simeq v_{t2}$, m/s	1980
Magnetoelastic coefficient, b_1, N/m^2	-34.3×10^6
Magnetoelastic coefficient, b_2, N/m^2	-359.4×10^6
Thermo-magneto-elastic coefficient A_1, MPa/K	-0.24
Thermo-magneto-elastic coefficient A_2, MPa/K	-2.6
Silica SiO_2 [36]	Value
Volumetric mass density ρ', kg/m^3	2196
Shear acoustic velocity, v'_t, m/s	3300
Longitudinal acoustic velocity, v'_l, m/s	5900

Figure 7 displays the spatial profile of the strains of Eq. (30) calculated for an effective laser fluence F of 2 mJ/cm^2, and a tilt angle θ of 7°. Let us underline that the effective fluence F of 2 mJ/cm^2 is calculated assuming that the terfenol optical reflectivity R is similar to that of iron, that lies in the range of 60%. Then, the effective fluence is calculated from $F = F_0(1 - R)$ where F_0 is the input laser fluence of about 5 mJ/cm^2 in our experiment. As emphasized in Fig. 7, the thermoelastic mechanism is much stronger than the demagnetostriction mechanism and of the same sign in this configuration. Note that since we are not sure about which crystallographic directions correspond to the positive or negative shear strains [(110) versus $(\bar{1}\bar{1}0)$ and $(1\bar{1}0)$ versus

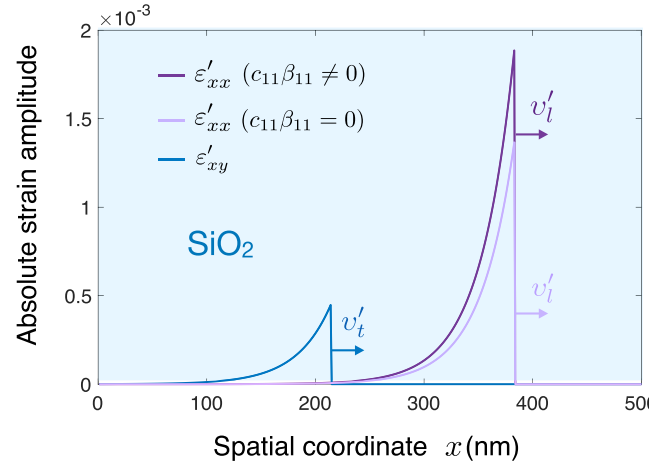

FIG. 7. Numerical simulations of the spatial distribution of the longitudinal ε'_{xx} and shear ε'_{xy} acoustic strains of Eqs. (30) and (31), at a time delay of 65 ps after laser-excitation, at a given effective fluence F of 2 mJ/cm^2, for a tilt angle of magnetization θ of 7°, and for an azimutal angle $\phi = 0$ that corresponds to $m_z = 0$ as well as $\varepsilon'_{xz} = 0$—the magnetization does not have any component along the hard axis. The longitudinal strain is calculated with the contribution of the thermoelastic effect ($c_{11}\beta_{11} \neq 0$) or without ($c_{11}\beta_{11} = 0$).

$(\bar{1}10)$], Fig. 7 displays the absolute value of the strain amplitudes. There is however no ambiguity about the thermoelastic longitudinal strain that should be of compressive nature (negative strain by convention). Since A_2 is negative, see Table I, and $m_x^2 - m_y^2 < 0$ at small θ angles, the thermoelastic and the magnetoelastic strains have the same sign, however, if the magnetization could be tilted further out-of-plane at substantial θ angles, these strains would have different signs and could compensate each other, leading to a weaker overall longitudinal strain. This competition between the longitudinal acoustic excitation through thermoelastic and magnetoelastic mechanisms could be verified experimentally at stronger external magnetic fields. Similarly to Ref. [50] that highlights the competition between inverse piezoelectricity and electron-deformation potential mechanisms, we would expect the longitudinal strain to vanish at a critical magnetic field that would balance the competing thermoelastic and magnetoelastic mechanisms.

Note that the detected acoustic pulses of Figs. 1(e) and 2(c) do not match the strain profiles simulated in Fig. 7 with a sharp discontinuity arising from the interface discontinuity, followed by a damped exponent profile arising from the optical penetration depth profile. There are several reasons for that (i) the strain pulses propagate back and forth through about 1-μm-thick SiO_2 layer. The acoustic damping smoothes the high frequency components of the strain discontinuity that spatially and temporally broadens; (ii) the optically measured signal intrinsically imply a convolution of the optical sensitivity function [24] with the acoustic strain profile. Thus, it is not only the strain profile that determines the final shape of the detected strains, but how the strain gets optically detected into the magnetic material as well, and more specifically to our MOKE detection scheme, how the acoustic strains cause the rotation of the probe polarization.

V. MAGNETOOPTICAL DETECTION OF STRAIN PULSES

As stated above, the detected magneto-optic dynamics related to the acoustic strains do not reflect accurately the acoustic strain profile. In fact, since the optical detection of the acoustic pulses is not δ-localized in space but rather spatially extended over the optical skin depth of the magnetostrictive sample, when the acoustic strains traveling in the SiO_2 dielectric layer gets transmitted back into the terfenol layer, it is the whole optical skin-depth area of Fig. 8(a) that contributes to the MOKE signal. The detected MOKE signal is therefore the integral of the acousto-magneto-optical response over the optical-skin depth area at every given time. Inspired by Ref. [24] that describes the change in optical reflectivity induced by the acoustic strain through the photoelastic effect, the MOKE optical detection of the acoustic strains can be modeled by assuming that time-resolved measured signals involve a convolution that reads,

$$\Delta\theta(t) \sim \int_0^\infty \varepsilon\left(t - \frac{\xi}{v_i'}\right) \exp^{-\alpha\xi} d\xi, \qquad (36)$$

where $\Delta\theta(t)$ is the time dependent rotation of the probe polarization, $\varepsilon(t + \frac{\xi}{v_i})$ any of the acoustic strains of Eqs. (30)–(32) that is transmitted back to the terfenol sample, and $\exp^{-\alpha\xi}$ is the magneto-optical detection profile determined by the optical penetration depth. Note that ξ in Eq. (36) is simply the inversion of the x axis, $\xi = -x$, to stress the fact that the acoustic strain travels back into the terfenol layer toward the negative x coordinates. In fact, unlike in Ref. [24] that introduces a so-termed sensitivity function, we assume that the convolution simply involves a damped exponent that matches the optical penetration depth of the probe light. The sensitivity function in Ref. [24] is useful to model complex photoelastic signals for which the detected acoustic strain pulses appear on the reflectivity data as intriguing bipolar or even multipolar pulses. Since the detected acoustic pulses of Fig. 1 are all of unipolar shape, and since the time duration of the acoustic pulses is relatively short, this approximation most probably stands fairly well [51]. To elaborate a full but rather complex analytical description of the magneto-optical detection of strain waves, tensorial calculations of the dielectric function involving the magneto-optic coefficients and the strains should be elaborated [52].

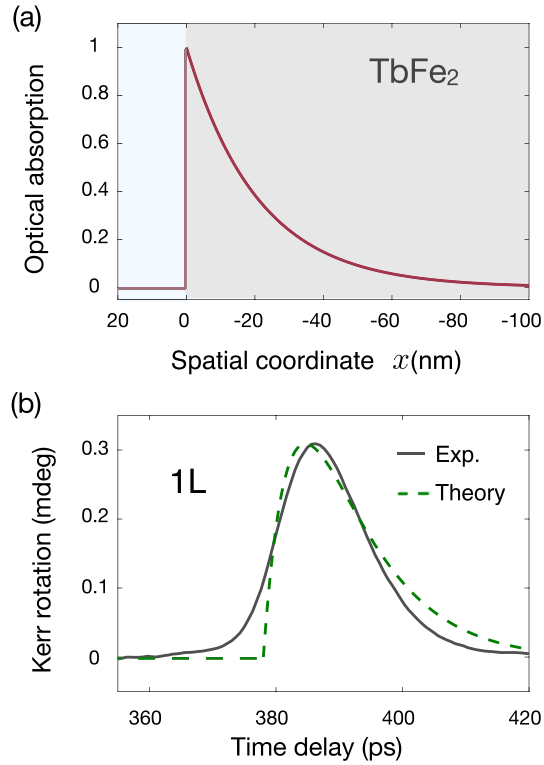

FIG. 8. (a) Optical absorption of the probe light beneath the SiO_2/$TbFe_2$ interface. (b) Theoretical and experimental MOKE signal corresponding to the unipolar longitudinal strain L of Figs. 1 and 2, analytically modeled in Fig. 7.

Figure 8(b) displays the numerical modeling from Eq. (36) of the MOKE detection of the longitudinal strain pulse L. The analytical MOKE signal modeled as a straightforward spatio-temporal convolution reproduce fairly well the experimental data. The FWHM duration of both experimental and theoretical strain pulses of about ~8 ps agree perfectly. Owing to the fact that our model does not take into account the acoustic damping in SiO_2, this rather simplistic modeling accurately reproduces the MOKE signal.

VI. SUMMARY

We have shown experimental results of ultrafast laser excitation of strain waves in highly magnetostrictive $TbFe_2$ epitaxial thin films. The excitation of these picosecond strain waves of longitudinal and shear acoustic polarizations is intrinsic to a direct magnetoelastic mechanism, referred as the demagnetostriction mechanism, which is linked to the laser-mediated release of the magnetostrictive built-in strains. We have introduced an analytical model for ultrafast strain pulses generation and detection in magnetostrictive materials, that can be extended to all class of magnetostrictive materials. Expressions of longitudinal and shear, static and dynamic strains, were developed. We demonstrate that the strain excitation is anisotropic and depends strongly on the magnetization vector orientation. We develop a theory for the MOKE detection of longitudinal and shear acoustic waves from the inverse magnetostriction mechanism. Note that since longitudinal and shear acoustic waves have different effects on the lattice (centro)symmetry, second harmonic generation (SHG) of strain waves [53,54] could be an interesting follow up. Overall, our work may become extremely relevant in the quest for efficient picosecond shear acoustic transducers that are seeking for a very long time. Being able to probe the ultrafast coupling between shear degrees of freedom and different material properties such as ferroelectricity, superconductivity and so on, would be extremely valuable.

ACKNOWLEDGMENTS

We gratefully acknowledge Agence Nationale de la Recherche for providing the financial support under grants ANR-14-CE26-0008 and ANR-16-CE30-0018, as well as European FET-Open funding under the acronyme Chiron. We are thankful to Matias Bargheer for many stimulating scientific discussions, to Lionel Guilmeau and Sébastien Nogarotto for extremely valuable technical support.

APPENDIX A: (110) MAGNETOSTRICTIVE SAMPLE

In case of a well-defined (110) single crystal, as in our experiments, all the energy term expressions are tensorial. Since the experimental coordinate system (x, y, z) does not correspond to the [100], [010], and [001] crystallographic directions, which form the conventional (x^*, y^*, z^*) coordinate system of textbooks for tensorial expressions, it is required to calculate the tensors upon a transformation of the coordinate system (x^*, y^*, z^*) into (x, y, z). Following [16], the (x, y, z) coordinate system is obtained from the (x^*, y^*, z^*) coordinate system from a clockwise rotation around the z axis by $\xi = \pi/4$. The corresponding rotation matrix have the form

$$[a] = \begin{bmatrix} \cos\xi & \sin\xi & 0 \\ -\sin\xi & \cos\xi & 0 \\ 0 & 0 & 1 \end{bmatrix}. \tag{A1}$$

Until the coordinate system is orthogonal, the elastic energy that couples the elastic constants with strains is invariant and can be expressed as

$$F_e = \tfrac{1}{2} c^*_{ijkl} \varepsilon^*_{ij} \varepsilon^*_{kl} = \tfrac{1}{2} c_{ijkl} \varepsilon_{ij} \varepsilon_{kl}, \tag{A2}$$

where $c^{(*)}_{ijkl}$ is the fourth rank elastic constants tensor and $\varepsilon^{(*)}_{ij}$ the two rank strain tensor [55]. The Einstein summation notation is used all along to imply summation over repeated indices and the superscript $*$ denotes the coordinate system (x^*, y^*, z^*). The calculation of the elastic energy in the coordinate system (x, y, z) is derived after rotation of the elastic tensor c^*_{ijkl} from the generic transformation equation of tensors,

$$c_{mnop} = a_{mi}\, a_{nj}\, a_{ok}\, a_{pl}\, c^*_{ijkl}. \tag{A3}$$

The calculation of each component of the transformed tensor with full subscripts notations is cumbersome. It is possible to adopt the abbreviated subscripts and transform the abbreviated tensor from the following equation:

$$[c] = [M][c^*][M]^t, \tag{A4}$$

where $[c^*]$ is the untransformed 6×6 elastic matrix in abbreviated form, as in any cubic system such as terfenol, it contains only three constants and reads

$$[c^*] = \begin{bmatrix} c_{11} & c_{12} & c_{12} & 0 & 0 & 0 \\ c_{12} & c_{11} & c_{12} & 0 & 0 & 0 \\ c_{12} & c_{12} & c_{11} & 0 & 0 & 0 \\ 0 & 0 & 0 & c_{44} & 0 & 0 \\ 0 & 0 & 0 & 0 & c_{44} & 0 \\ 0 & 0 & 0 & 0 & 0 & c_{44} \end{bmatrix}. \tag{A5}$$

$[M]$ and $[M]^t$ in Eq. (A4) are the transformation and transposed transformation matrices, respectively. These matrices termed Bond matrices can be calculated analytically as in Ref. [55],

$$[M] = \begin{bmatrix} a_{11}^2 & a_{12}^2 & a_{13}^2 & 2a_{12}a_{13} & 2a_{13}a_{11} & 2a_{11}a_{12} \\ a_{21}^2 & a_{22}^2 & a_{23}^2 & 2a_{22}a_{23} & 2a_{23}a_{21} & 2a_{21}a_{22} \\ a_{31}^2 & a_{32}^2 & a_{33}^2 & 2a_{32}a_{33} & 2a_{33}a_{31} & 2a_{31}a_{32} \\ a_{21}a_{31} & a_{22}a_{32} & a_{23}a_{33} & a_{22}a_{33}+a_{23}a_{32} & a_{21}a_{33}+a_{23}a_{31} & a_{22}a_{31}+a_{21}a_{32} \\ a_{31}a_{11} & a_{32}a_{12} & a_{33}a_{13} & a_{12}a_{33}+a_{13}a_{32} & a_{13}a_{31}+a_{11}a_{33} & a_{11}a_{32}+a_{12}a_{31} \\ a_{11}a_{21} & a_{12}a_{22} & a_{13}a_{23} & a_{12}a_{23}+a_{13}a_{22} & a_{13}a_{21}+a_{11}a_{23} & a_{11}a_{22}+a_{12}a_{21} \end{bmatrix}. \tag{A6}$$

In the specific case of a rotation matrix such as in Eq. (A1), it simplifies to

$$[M(\xi)] = \begin{bmatrix} \cos^2\xi & \sin^2\xi & 0 & 0 & 0 & \sin 2\xi \\ \sin^2\xi & \cos^2\xi & 0 & 0 & 0 & -\sin 2\xi \\ 0 & 0 & 1 & 0 & 0 & 0 \\ 0 & 0 & 0 & \cos\xi & -\sin\xi & 0 \\ 0 & 0 & 0 & \sin\xi & \cos\xi & 0 \\ -\frac{1}{2}\sin 2\xi & \frac{1}{2}\sin 2\xi & 0 & 0 & 0 & \cos 2\xi \end{bmatrix}, \tag{A7}$$

and for a rotation angle $\xi = \pi/4$, it simplifies further to

$$[M(\pi/4)] = \begin{bmatrix} \frac{1}{2} & \frac{1}{2} & 0 & 0 & 0 & 1 \\ \frac{1}{2} & \frac{1}{2} & 0 & 0 & 0 & -1 \\ 0 & 0 & 1 & 0 & 0 & 0 \\ 0 & 0 & 0 & \frac{1}{\sqrt{2}} & -\frac{1}{\sqrt{2}} & 0 \\ 0 & 0 & 0 & \frac{1}{\sqrt{2}} & \frac{1}{\sqrt{2}} & 0 \\ -\frac{1}{2} & \frac{1}{2} & 0 & 0 & 0 & 0 \end{bmatrix}. \tag{A8}$$

The transposed matrix of this last expression is straightforward. The matrix product of Eq. (A4) lead to the transformed matrix of the elastic constants $[c]$ in the coordinate system (x, y, z),

$$[c] = \begin{bmatrix} c'_{11} & c'_{12} & c_{12} & 0 & 0 & 0 \\ c'_{12} & c'_{11} & c_{12} & 0 & 0 & 0 \\ c_{12} & c_{12} & c_{11} & 0 & 0 & 0 \\ 0 & 0 & 0 & c_{44} & 0 & 0 \\ 0 & 0 & 0 & 0 & c_{44} & 0 \\ 0 & 0 & 0 & 0 & 0 & \frac{c_{11}-c_{12}}{2} \end{bmatrix}, \tag{A9}$$

where

$$c'_{11} = \frac{c_{11}+c_{12}}{2} + c_{44}, \qquad c'_{12} = \frac{c_{11}+c_{12}}{2} - c_{44},$$

Finally, using Eqs. (1) and (A2), the elastic energy F_e written in the (x, y, z) coordinate system have the form

$$F_e = \frac{1}{2}\left[\left(\frac{c_{11}+c_{12}}{2} + c_{44}\right)\varepsilon_{xx}^2 + 2(c_{11}-c_{12})\,\varepsilon_{xy}^2 + 4\,c_{44}\,\varepsilon_{xz}^2\right]. \tag{A10}$$

In the most general case for which magnetostriction is the dominant magnetoelastic effect in the compound, the general tensorial expression for the magnetoelastic energy is quadratic with magnetization and follows:

$$F_{\text{me}} = b^*_{ijkl}\varepsilon^*_{ij}m^*_k m^*_l, \tag{A11}$$

where b_{ijkl} is the fourth-rank magnetoelastic tensor written in the (x^*, y^*, z^*) coordinate system [42]. For instance, in case of cubic crystals of $\bar{4}3m$, 432, and $m\bar{3}m$ point groups, the b^*_{ijkl} tensor can be written in a contracted form as a 6×6 matrix that reads [57]

$$[b^*] = \begin{bmatrix} b_{11} & b_{12} & b_{12} & 0 & 0 & 0 \\ b_{12} & b_{11} & b_{12} & 0 & 0 & 0 \\ b_{12} & b_{12} & b_{11} & 0 & 0 & 0 \\ 0 & 0 & 0 & b_{44} & 0 & 0 \\ 0 & 0 & 0 & 0 & b_{44} & 0 \\ 0 & 0 & 0 & 0 & 0 & b_{44} \end{bmatrix}, \tag{A12}$$

for which $b_{pq} = b_{ijkl}$ for $q = 1, 2, 3$, and $b_{pq} = 2\,b_{ijkl}$ for $q = 4, 5, 6$. In the contracted form, the tensorial expression of the magnetoelastic energy can be written in the form

$$F_{\text{me}} = b^*_{pq}\varepsilon^*_p(m^*m^*)_q. \tag{A13}$$

Eventhough the symmetry rules of the fourth-rank magnetoelastic tensor are identical to others fourth-rank tensors such as the photoelastic tensor [56], the tensor transformation in the contracted form is elusive and sometimes contradictory in the literature [42,57]. For this reason, rather than transforming the magnetoelastic tensor, we will expand the magnetoelastic energy expressed in the (x^*, y^*, z^*) coordinate system and transform the strains ε^* and the unit vector of magnetization m^* in the (x, y, z) coordinate system.

After some calculation based on Eq. (A12) and (A13), and taking into account that $m^{*2}_x + m^{*2}_y + m^{*2}_z = 1$, we obtain the rather conventional magnetoelastic energy in case of cubic symmetry [33,58–60]:

$$F_{\text{me}} = b_1\left(m^{*2}_x\varepsilon^*_{xx} + m^{*2}_y\varepsilon^*_{yy} + m^{*2}_z\varepsilon^*_{zz}\right) + b_2(m^*_x m^*_y\varepsilon^*_{xy} + m^*_x m^*_z\varepsilon^*_{xz} + m^*_y m^*_z\varepsilon^*_{yz}), \tag{A14}$$

where the magnetoelastic constants b_1 and b_2 follow $b_1 = b_{11} - b_{12}$, $b_2 = b_{44}$.

In order to express the strains ε^*_{ij} as a combination of the strains ε_{kl}, it is required to rotate the (x, y, z) coordinate system around the z-axis by $\xi = -\pi/4$, in reverse direction as previously in Eq. (A7). In contracted notations, it follows:

$$\varepsilon^* = [M(-\pi/4)]\,\varepsilon, \tag{A15}$$

where $[M(-\pi/4)]$ is the Bond matrix $[M]$ of Eq. (A7) with $\xi = -\pi/4$. We recall that the only nonzero strains in contracted notations are $\varepsilon_1 = \varepsilon_{11}$, $\varepsilon_6 = 2\,\varepsilon_{12}$ and $\varepsilon_5 = 2\,\varepsilon_{13}$. After calculations, we obtain the following set of equations:

$$\varepsilon^*_{xx} = \frac{1}{2}\varepsilon_{xx} - 2\varepsilon_{xy}, \quad \varepsilon^*_{yy} = \frac{1}{2}\varepsilon_{xx} + 2\varepsilon_{xy}, \quad \varepsilon^*_{zz} = 0,$$
$$\varepsilon^*_{yz} = \frac{1}{\sqrt{2}}\varepsilon_{xz}, \quad \varepsilon^*_{xz} = \frac{1}{\sqrt{2}}\varepsilon_{xz}, \quad \varepsilon^*_{xy} = \frac{1}{4}\varepsilon_{xx}, \tag{A16}$$

As for the unit vector of magnetization m_i^*, it follows:

$$m_x^* = \frac{1}{\sqrt{2}}(m_x - m_y),\ \ m_y^* = \frac{1}{\sqrt{2}}(m_x + m_y),$$
$$m_z^* = m_z. \tag{A17}$$

Finally, from Eq. (A14), (A16), and (A17), we calculate the magnetoelastic energy expressed in the coordinate system (x, y, z) that takes the form

$$F_{\text{me}} = b_1\left(\frac{1}{2}\left(m_x^2 + m_y^2\right)\varepsilon_{xx} + 4m_x m_y \varepsilon_{xy}\right)$$
$$+b_2\left(\frac{1}{8}\left(m_x^2 - m_y^2\right)\varepsilon_{xx} + m_x m_z \varepsilon_{xz}\right). \tag{A18}$$

APPENDIX B: (111) MAGNETOSTRICTIVE SAMPLE

The built-in magnetostrictive strains, in case of a magnetostrictive sample with (111) out-of-plane crystallographic direction, can be found in a similar way as in Sec. IV A by minimizing the elastic and magnetoelastic free energy density. After calculations, these strains read,

$$\varepsilon_{xx} = \frac{(b_1 - b_2)\left(3m_x^2 + m_y^2 + 2m_z^2 + 2\sqrt{2}m_x m_z\right)}{c_{11} - (c_{12} + c_{44})/3}, \tag{B1}$$

$$\varepsilon_{xy} = \frac{2(b_1 - b_2)(1/3m_x m_y - 2/3\sqrt{2}m_y m_z)}{(c_{11} + c_{12})/4 + c_{44}}, \tag{B2}$$

$$\varepsilon_{xz} = -\frac{4(b_1 - b_2)\left(1/\sqrt{2}m_y^2 + 1/3m_x m_z\right)}{c_{11} + c_{12} + c_{44}}. \tag{B3}$$

Interestingly, at the contrary to the (110) sample, in that case, there is an additional quadratic term m_y^2 that appears in Eq. (B3), which means that under some really specific circumstances of the magnetization direction, the shear built-in strain does not change sign upon reversal of the magnetization.

[1] E. Beaurepaire, J.-C. Merle, A. Daunois, and J.-Y. Bigot, Ultrafast Spin Dynamics in Ferromagnetic Nickel, Phys. Rev. Lett. **76**, 4250 (1996).

[2] M. Aeschlimann, M. Bauer, S. Pawlik, W. Weber, R. Burgermeister, D. Oberli, and H. C. Siegmann, Ultrafast Spin-dependent Electron Dynamics in Fcc Co, Phys. Rev. Lett. **79**, 5158 (1997).

[3] A. Scholl, L. Baumgarten, R. Jacquemin, and W. Eberhardt, Ultrafast Spin Dynamics of Ferromagnetic thin Films Observed by fs Spin-resolved Two-photon Photoemission, Phys. Rev. Lett. **79**, 5146 (1997).

[4] J.-Y. Bigot, M. Vomir, and E. Beaurepaire, Coherent ultrafast magnetism induced by femtosecond laser pulses, Nat. Phys. **5**, 515 (2009).

[5] C. Boeglin, E. Beaurepaire, V. Halté, V. López-Flores, C. Stamm, N. Pontius, H. A. Dürr, and J.-Y. Bigot, Distinguishing the ultrafast dynamics of spin and orbital moments in solids, Nature (London) **465**, 458 (2010).

[6] T. Nova, A. Cartella, A. Cantaluppi, M. Forst, D. Bossini, R. Mikhaylovskiy, A. Kimel, R. Merlin, and A. Cavalleri, An effective magnetic field from optically driven phonons, Nat. Phys. **13**, 132 (2017).

[7] A. Disa, M. Fechner, T. Nova, B. Liu, M. Forst, D. Prabhakaran, P. Radaelli, and A. Cavalleri, Polarizing an antiferromagnet by optical engineering of the crystal field, Nat. Phys. **16**, 937 (2020).

[8] B. Koopmans, G. Malinowski, F. Dalla Longa, D. Steiauf, M. Fähnle, T. Roth, M. Cinchetti, and M. Aeschlimann, Explaining the paradoxical diversity of ultrafast laser-induced demagnetization, Nat. Mater. **9**, 259 (2010).

[9] A. Kirilyuk, A. V. Kimel, and T. Rasing, Ultrafast optical manipulation of magnetic order, Rev. Mod. Phys. **82**, 2731 (2010).

[10] C. D. Stanciu, F. Hansteen, A. V. Kimel, A. Kirilyuk, A. Tsukamoto, A. Itoh, and T. Rasing, All-Optical Magnetic Recording with Circularly Polarized Light, Phys. Rev. Lett. **99**, 047601 (2007).

[11] A. Hassdenteufel, B. Hebler, C. Schubert, A. Liebig, M. Teich, M. Helm, M. Aeschlimann, M. Albrecht, and R. Bratschitsch, Thermally assisted all-optical helicity dependent magnetic switching in amorphous $Fe_{100-x}Tb_x$ alloy films, Adv. Mater. **25**, 3122 (2013).

[12] S. Mangin, M. Gottwald, C.-H. Lambert, D. Steil, V. Uhlir, L. Pang, M. Hehn, S. Alebrand, M. Cinchetti, G. Malinowski, Y. Fainman, M. Aeschlimann, and E. Fullerton, Engineered materials for all-optical helicity-dependent magnetic switching, Nat. Mater. **13**, 286 (2014).

[13] A. Scherbakov, A. Salasyuk, A. Akimov, X. Liu, M. Bombeck, C. Brüggemann, D. Yakovlev, V. Sapega, J. Furdyna, and M. Bayer, Coherent Magnetization Precession in Ferromagnetic (Ga, Mn)As Induced by Picosecond Acoustic Pulses, Phys. Rev. Lett. **105**, 117204 (2010).

[14] L. Thevenard, E. Peronne, C. Gourdon, C. Testelin, M. Cubukcu, E. Charron, S. Vincent, A. Lemaître, and B. Perrin, Effect of picosecond strain pulses on thin layers of the ferromagnetic semiconductor (Ga, Mn)(As, P), Phys. Rev. B **82**, 104422 (2010).

[15] J.-W. Kim, M. Vomir, and J.-Y. Bigot, Ultrafast Magnetoacoustics in Nickel Films, Phys. Rev. Lett. **109**, 166601 (2012).

[16] O. Kovalenko, T. Pezeril, and V. V. Temnov, New Concept for Magnetization Switching by Ultrafast Acoustic Pulses, Phys. Rev. Lett. **110**, 266602 (2013).

[17] A. H. Reid, X. Shen, P. Maldonado, T. Chase, E. Jal, P. W. Granitzka, K. Carva, R. K. Li, J. Li, L. Wu *et al.*, Beyond a phenomenological description of magnetostriction, Nat. Commun. **9**, 388 (2018).

[18] A. Stupakiewicz, C. Davies, K. Szerenos, D. Afanasiev, K. Rabinovich, A. Boris, A. Caviglia, A. Kimel, and A. Kirilyuk, Ultrafast phononic switching of magnetization, Nat. Phys. **17**, 489 (2021).

[19] D. Afanasiev, J. Hortensius, B. Ivanov, A. Sasani, E. Bousquet, Y. Blanter, R. Mikhaylovskiy, A. Kimel, and A. Caviglia, Ultrafast control of magnetic interactions via light-driven phonons, Nat. Mater. **20**, 607 (2021).

[20] D. Marwan, E. Popova, S. Zeuschner, W. Leitenberger, N. Keller, M. Rössle, and M. Bargheer, Ultrafast control of

lattice strain via magnetic circular dichroism, Phys. Rev. B **103**, 064301 (2021).

[21] S. Zeuschner, T. Parpiiev, T. Pezeril, A. Hillion, K. Dumesnil, A. Anane, J. Pudell, L. Willig, M. Rössle, M. Herzog, A. von Reppert, and M. Bargheer, Tracking picosecond strain pulses in heterostructures that exhibit giant magnetostriction, Struct. Dyn. **6**, 024302 (2019).

[22] A. von Reppert, M. Mattern, J.-E. Pudell, S. P. Zeuschner, K. Dumesnil, and M. Bargheer, Unconventional picosecond strain pulses resulting from the saturation of magnetic stress within a photoexcited rare earth layer, Struct. Dyn. **7**, 024303 (2020).

[23] A. von Reppert, L. Willig, J.-E. Pudell, S. Zeuschner, G. Sellge, F. Ganss, O. Hellwig, J. Arregi, V. Uhlir, A. Crut, and M. Bargheer, Spin stress contribution to the lattice dynamics of FePt, Sci. Adv. **6**, 1142 (2020).

[24] C. Thomsen, H. Grahn, H. Maris, and J. Tauc, Surface generation and detection of phonons by picosecond light pulses, Phys. Rev. B **34**, 4129 (1986).

[25] P. Ruello and V. E. Gusev, Physical mechanisms of coherent acoustic phonons generation by ultrafast laser action, Ultrasonics **56**, 21 (2015).

[26] T. Pezeril, Laser generation and detection of ultrafast shear acoustic waves in solids and liquids, Opt. Laser Tech. **83**, 177 (2016).

[27] C. Dornes, Y. Acremann, M. Savoini *et al.*, The ultrafast Einstein-de Haas effect, Nature (London) **565**, 209212 (2019).

[28] T. Pezeril, C. Klieber, S. Andrieu, and K. Nelson, Optical Generation of Gigahertz-frequency Shear Acoustic Waves in Liquid Glycerol, Phys. Rev. Lett. **102**, 107402 (2009).

[29] A. Clark, in *Handbook on the Physics and Chemistry of Rare Earths* (Elsevier, Amsterdam, 1979), Vol. 2, Chap. 15, pp. 231–258.

[30] M. Wietstruk, A. Melnikov, C. Stamm, T. Kachel, N. Pontius, M. Sultan, C. Gahl, M. Weinelt, H. A. Dürr, and U. Bovensiepen, Hot-Electron-Driven Enhancement of Spin-lattice Coupling in Gd and Tb 4*f* Ferromagnets Observed by Femtosecond X-ray Magnetic Circular Dichroism, Phys. Rev. Lett. **106**, 127401 (2011).

[31] T. Parpiiev, Ultrafast magneto-acoustics in magnetostrictive materials, Ph.D. thesis, https://hal.archives-ouvertes.fr/tel-01798696.

[32] V. Oderno, C. Dufour, K. Dumesnil, P. Mangin, and G. Marchal, Epitaxial growth of (110) $DyFe_2$, $TbFe_2$ and $Dy_{0.7}Tb_{0.3}Fe_2$ thin films by molecular beam epitaxy, J. Cryst. Growth **165**, 175 (1996).

[33] A. Mougin, C. Dufour, K. Dumesnil, and Ph. Mangin, Strain-induced magnetic anisotropy in single-crystal RFe_2 (110) thin films (R=Dy, Er, Tb, $Dy_{0.7}Tb_{0.3}$, Sm, Y), Phys. Rev. B **62**, 9517 (2000).

[34] R. Bruckner, Properties and structure of vitreous silica, J. Non-Cryst. Solids **5**, 123 (1970).

[35] J.-W. Kim, K.-D. Lee, J.-W. Jeong, and S.-C. Shin, Ultrafast spin demagnetization by nonthermal electrons of TbFe alloy film, Appl. Phys. Lett. **94**, 192506 (2009).

[36] O. Matsuda, O. Wright, D. H. Hurley, V. Gusev, and K. Shimizu, Coherent shear phonon generation and detection with picosecond laser acoustics, Phys. Rev. B **77**, 224110 (2008).

[37] A. Clark, R. Abbundi, H. Savage, and O. McMasters, Magnetostriction of rare earth-Fe_2 laves phase compounds, Physica B+C **86-88**, 73 (1977).

[38] Z. Chen, S. Li, S. Zhou, and T. Lai, Ultrafast dynamics of 4f electron spins in TbFeCo film driven by inter-atomic 3d-5d-4f exchange coupling, New J. Phys. **21**, 123007 (2019).

[39] A. Bonda, L. Uba, K. Załęski, and S. Uba, Ultrafast magnetization dynamics in an epitaxial $Ni_{54.3}Mn_{31.9}Sn_{13.8}$ Heusler-alloy film close to the Curie temperature, Phys. Rev. B **99**, 184424 (2019).

[40] T. Roth, A. Schellekens, S. Alebrand, O. Schmitt, D. Steil, B. Koopmans, M. Cinchetti, and M. Aeschlimann, Temperature Dependence of Laser-Induced Demagnetization in Ni: A Key For Identifying The Underlying Mechanism, Phys. Rev. X **2**, 021006 (2012).

[41] J. Liu, F. de Boer, P. de Câhtel, R. Coehoorn, and K. Buschow, On the 4f-3d exchange interaction in intermetallic compounds, J. Magn. Magn. Mater **132**, 159 (1994).

[42] R. Le Craw and R. Comstock, in *Physical Acoustics*, edited by W. P. Mason (Academic Press, New York, 1965), Vol. 3, Part B, Chap. 4.

[43] S. Rinaldi, J. Cullen, and G. Blessing, Magnetoelastic coupling in $Tb_{0.3}Dy_{0.7}Fe_2$ measured ultrasonically, Phys. Lett. A **61**, 465 (1977).

[44] P. Hansen and R. Krishnan, Anisotropy and magnetostriction of 4d and 5d transition-metal ions in garnets and spinel ferrites, J. Phys. Colloq. **38**, 147 (1977).

[45] C.-K. Min, D. Cahill, and S. Granick, Time-resolved ellipsometry for studies of heat transfer at liquid/solid and gas/solid interfaces, Rev. Sci. Instrum. **81**, 074902 (2010).

[46] T. Pezeril, P. Ruello, S. Gougeon, N. Chigarev, D. Mounier, J.-M. Breteau, P. Picart, and V. Gusev, Generation and detection of plane coherent shear picosecond acoustic pulses by lasers: experiment and theory, Phys. Rev. B **75**, 174307 (2007).

[47] J. Adams, D. Agosta, R. Leisure, and H. Ledbetter, Elastic constants of monocrystal iron from 3 to 500 K, J. Appl. Phys. **100**, 113530 (2006).

[48] L. Sandlund, M. Fahlander, T. Cedell, A. E. Clark, J. B. Restorff, and M. WunFogle, Magnetostriction, elastic moduli, and coupling factors of composite terfenol-D, J. Appl. Phys. **75**, 5656 (1994).

[49] L. Garcia-Gancedo, S. C. Busbridge, P. Pernod, and V. Preobrazhensky, Magnetoacoustic properties of self-biased terfenol-D 2-2 composites, J. Appl. Phys. **101**, 09C514 (2007).

[50] G. Vaudel, T. Pezeril, A. Lomonosov, M. Lejman, P. Ruello, and V. Gusev, Laser generation of hypersound by a terahertz photo-Dember electric field in a piezoelectric GaAs semiconductor, Phys. Rev. B **90**, 014302 (2014).

[51] K. Manke, A. Maznev, C. Klieber, V. Shalagatskyi, V. Temnov, D. Makarov, S.-H. Baek, C.-B. Eom, and K. Nelson, Measurement of shorter-than-skin-depth acoustic pulses in a metal film via transient reflectivity, Appl. Phys. Lett. **103**, 173104 (2013).

[52] J. Zak, R. Moog, C. Liu, and S. Bader, Universal approach to magneto-optics, J. Magn. Magn. Mater. **89**, 107 (1990).

[53] H. Zhao, Y. Fan, G. Lupke, A. Hanbicki, C. Li, and B. Jonker, Detection of coherent acoustic phonons by time-resolved second-harmonic generation, Phys. Rev. B **83**, 212302 (2011).

[54] L. Huber, A. Ferrer, T. Kubacka, T. Huber, C. Dornes, T. Sato, K. Ogawa, K. Tono, T. Katayama, Y. Inubushi, M. Yabashi, Y.

Tanaka, P. Beaud, M. Fiebig, V. Scagnoli, U. Staub, and S. L. Johnson, Coherent acoustic perturbation of second-harmonic generation in NiO, Phys. Rev. B **92**, 094304 (2015).

[55] B. A. Auld, *Acoustic Fields and Waves in Solids* (Wiley, New York, 1973).

[56] J. Nye, *Physical Properties of Crystals* (Oxford University Press, New York, 2001).

[57] V. Lemanov, in *Physics of Magnetic Dielectrics* (Nauka, Leningrad, 1974), p. 299.

[58] C. de la Fuente, J. Arnaudas, L. Benito, M. Ciria, A. del Moral, C. Dufour, and K. Dumesnil, Magnetocrystalline anisotropy in a (110) $(Tb_{0.27}Dy_{0.73})Fe_2$ thin-film, J. Phys.: Condens. Matter **16**, 2959 (2004).

[59] T. Linnik, A. Scherbakov, D. Yakovlev, X. Liu, J. Furdyna, and M. Bayer, Theory of magnetization precession induced by a picosecond strain pulse in ferromagnetic semiconductor (Ga, Mn)As, Phys. Rev. B **84**, 214432 (2011).

[60] V. Kats, T. Linnik, A. Salasyuk, A. Rushforth, M. Wang, P. Wadley, A. Akimov, S. Cavill, V. Holy, A. Kalashnikova, and A. Scherbakov, Ultrafast changes of magnetic anisotropy driven by laser-generated coherent and noncoherent phonons in metallic films, Phys. Rev. B **93**, 214422 (2016).